



CHORUS

This is the accepted manuscript made available via CHORUS. The article has been published as:

Reconstruction of phonon relaxation times from systems featuring interfaces with unknown properties

Mojtaba Forghani and Nicolas G. Hadjiconstantinou

Phys. Rev. B **97**, 195440 — Published 24 May 2018

DOI: [10.1103/PhysRevB.97.195440](https://doi.org/10.1103/PhysRevB.97.195440)

Reconstruction of phonon relaxation times from systems featuring interfaces with unknown properties

Mojtaba Forghani and Nicolas G. Hadjiconstantinou,
Department of Mechanical Engineering, Massachusetts Institute of Technology
Cambridge, MA 02139, USA

May 11, 2018

Abstract

We present a method for reconstructing the phonon relaxation time function $\tau_\omega = \tau(\omega)$ (including polarization) and associated phonon free path distribution from thermal spectroscopy data for systems featuring interfaces with unknown properties. Our method does not rely on the effective thermal conductivity approximation or a particular physical model of the interface behavior. The reconstruction is formulated as an optimization problem in which the relaxation times are determined as functions of frequency by minimizing the discrepancy between the experimentally measured temperature profiles and solutions of the Boltzmann transport equation for the same system. Interface properties such as transmissivities are included as unknowns in the optimization; however, because for the thermal spectroscopy problems considered here the reconstruction is not very sensitive to the interface properties, the transmissivities are only approximately reconstructed and can be considered as byproducts of the calculation whose primary objective is the accurate determination of the relaxation times. The proposed method is validated using synthetic experimental data obtained from Monte Carlo solutions of the Boltzmann transport equation. The method is shown to remain robust in the presence of uncertainty (noise) in the measurement.

1 Introduction

The study of phonon relaxation-time and free-path distributions has received considerable attention [1–7] in the context of nanoscale solid-state heat transport. This information is required for modeling heat transport at the kinetic level, which becomes necessary due to the failure of Fourier-based analyses at such small scales. Example applications include improved heat management in nanoelectronic circuits and devices [8–12] and nano-structured materials for improved thermoelectric conversion efficiency [13–18].

Thermal spectroscopy [5, 7] has emerged as a promising method for experimentally “extracting” the phonon free path distribution in a crystalline material. However, the analysis of thermal spectroscopy data remains a challenging task. To extract the free

path distribution from the experimentally measured temperature relaxation profiles, researchers typically invoke the concept of “effective thermal conductivity” and proceed to match the experimentally measured response to solutions of the heat conduction equation with the thermal conductivity (or thermal diffusivity) treated as an adjustable, “effective” property [5, 7]. Unfortunately, as we have shown in [19], this procedure implicitly assumes that heat transport is Fourier-like, which is only justified under fairly restrictive conditions (late times and large scales) that are not always satisfied under experimental conditions.

In order to address this limitation, in a previous paper [19] we proposed a technique for reconstructing phonon relaxation times which does not assume validity of Fourier’s law and does not make use of the effective thermal conductivity concept. In the proposed technique, reconstruction was posed as an optimization problem in which the relaxation time distribution is obtained as the distribution of relaxation times that minimizes the error between experimentally measured material response and the one obtained from the Boltzmann transport equation (BTE) solutions (numerical or analytical). This method has been validated using synthetically generated temperature profiles in the transient thermal grating (TTG) geometry [4, 20, 21], using both deviational Monte Carlo (MC) simulations [22–25] and inverse fast Fourier transform (IFFT) algorithms, in the presence and absence of noise in the measurement, on two different sets of silicon material properties [19].

Due to the ubiquity of solid-solid interfaces in nano-structures [26–28] and thermal spectroscopy experiments [7, 29] in particular, in the present paper we extend our approach to thermal spectroscopy problems in which a material interface is present. More specifically, we use an extended version of the optimization algorithm proposed previously [19], where frequency-dependent interface transmissivities are treated as unknowns of the optimization problem along with the frequency-dependent relaxation times. In other words, no assumption of underlying Fourier-like transport is made, in contrast to previous approaches which typically treat problems with interfaces by introducing an *assumed known* thermal boundary resistance [30] to the Fourier-based, effective thermal conductivity formulation [7].

We validate the proposed methodology using deviational MC-generated synthetic relaxation profiles of time domain thermoreflectance (TDTR) experiments in the 2D-dots geometry for an Al-Si system, similar to the experimental setup used in [7]. We find that the relaxation time/free path distribution can be obtained with good accuracy despite the additional unknowns introduced by the interface description. This is partly due to the fact that accurate *relaxation-time reconstruction* does not require determination of the interface properties to the same accuracy level and thus the number of unknowns introduced by the interface model can be kept small. The latter finding, namely that the reconstruction of the relaxation time/free path distribution can be achieved without reconstructing the interface properties at the same level of accuracy, is of great consequence for thermal spectroscopy applications where reconstruction of the relaxation times is the primary interest, as is the case here, because it implies that

a number of reconstructions previously thought intractable are, in fact, feasible. Our results also indicate that the accuracy of the reconstructed relaxation times is fairly insensitive to the transport regime and properties of the metal dot used in the thermal spectroscopy experiment (Al in the present case)

The remainder of the paper is organized as follows. In section 2, we formulate the reconstruction as an optimization problem requiring only solutions of the BTE and present the optimization framework used for the reconstruction. In section 3, we discuss the implementation of the algorithm. In section 4, we validate the proposed methodology using synthetic experimental data for the 2D-dots geometry [7], discuss our results and compare our method to previously used effective thermal conductivity-based approaches. Finally, in section 5 we provide a summary of our work and suggestions for future improvements.

2 Formulation

2.1 Governing equations

Phonon-mediated heat transport in thermal spectroscopy experiments can be described by the linearized Boltzmann transport equation (BTE)

$$\frac{\partial e^d}{\partial t} + \mathbf{v}_\omega \cdot \nabla_{\mathbf{x}} e^d = -\frac{e^d - (de^{\text{eq}}/dT)_{T_{\text{eq}}} \Delta \tilde{T}}{\tau_\omega}, \quad (1)$$

where $e^d = e^d(t, \mathbf{x}, \omega, \boldsymbol{\Omega}) = e - e_{T_{\text{eq}}}^{\text{eq}} = \hbar\omega(f - f_{T_{\text{eq}}}^{\text{eq}})$ is the deviational energy distribution, ω is the phonon frequency (including polarization), $\boldsymbol{\Omega}$ is the phonon traveling direction, $f = f(t, \mathbf{x}, \omega, \boldsymbol{\Omega})$ is the occupation number of phonon modes, $\mathbf{v}_\omega = \mathbf{v}(\omega)$ is the phonon group velocity, $\tau_\omega = \tau(\omega)$ is the frequency-dependent relaxation time, and \hbar is the reduced Planck constant. In general, $\tau_\omega = \tau(\omega, T)$; however, as a result of the linearization due to small temperature differences associated with thermal spectroscopy setups, $\tau_\omega = \tau(\omega, T_{\text{eq}}) \equiv \tau(\omega)$; in other words, the BTE is written here for the experiment baseline temperature T_{eq} . Also, $(de^{\text{eq}}/dT)_{T_{\text{eq}}} = \hbar\omega(df_T^{\text{eq}}/dT)|_{T_{\text{eq}}}$ and f_T^{eq} is the Bose-Einstein distribution with temperature parameter T , given by

$$f_T^{\text{eq}}(\omega) = \frac{1}{\exp(\hbar\omega/k_B T) - 1}, \quad (2)$$

where k_B is Boltzmann's constant. In the above, $\tilde{T}(t, \mathbf{x})$ is the pseudo-temperature and $\Delta \tilde{T} = \Delta \tilde{T}(t, \mathbf{x}) = \tilde{T} - T_{\text{eq}}$ is referred to as the deviational pseudo-temperature (different from the deviational temperature ΔT) which can be obtained using the energy conservation statement [24]

$$\int_{\boldsymbol{\Omega}} \int_{\omega} \left[\frac{C_\omega}{\tau_\omega} \Delta \tilde{T} - \frac{e^d}{\tau_\omega} D_\omega \right] d\omega d\boldsymbol{\Omega} = 0, \quad (3)$$

in which $D_\omega = D(\omega)$ is the density of states, $C_\omega = C(\omega; T_{\text{eq}}) = D_\omega(de^{\text{eq}}/dT)_{T_{\text{eq}}}$ is the frequency-dependent volumetric heat capacity, and $d\Omega = \sin(\theta)d\theta d\phi$ is the differential solid angle element where θ and ϕ are the polar and azimuthal angles in the spherical coordinate system, respectively. The temperature $T(t, \mathbf{x})$ ($\Delta T(t, \mathbf{x}) = T - T_{\text{eq}}$ is the deviational temperature) is related to the deviational energy via

$$\int_{\Omega} \int_{\omega} [C_\omega \Delta T - e^{\text{d}} D_\omega] d\omega d\Omega = 0. \quad (4)$$

The frequency-dependent free path is given by

$$\Lambda_\omega = v_\omega \tau_\omega, \quad (5)$$

where $v_\omega = \|\mathbf{v}_\omega\|$ is the frequency-dependent group velocity magnitude.

In the presence of a material interface, equation (1) requires matching conditions across the interface, usually supplied in the form of phonon transmissivities. More specifically, the frequency-dependent transmissivity from material 1 to material 2 in the presence of interface in a given geometry, denoted by $T_{12,\omega}$, is defined as the probability that a phonon with frequency ω can transmit through the interface. Similarly, the reflectivity, $R_{12,\omega} = 1 - T_{12,\omega}$, is the probability that the phonon is reflected back into material 1 after impinging on the interface. In this work, we have assumed elastic and diffuse scattering (at the interface), that is, phonons preserve their mode as they travel across the interface while losing the memory of their initial direction (emerging direction is random). Under these assumptions, the transmissivities of two sides of the interface are related to each other through the principle of detailed balance [31],

$$T_{12,\omega} v_{\omega,1} C_{\omega,1} = T_{21,\omega} v_{\omega,2} C_{\omega,2} \quad (6)$$

where $C_{\omega,1}$ and $v_{\omega,1}$ are the frequency-dependent volumetric heat capacity and group velocity of material 1 and similarly $C_{\omega,2}$ and $v_{\omega,2}$ are the frequency-dependent volumetric heat capacity and group velocity of material 2. The transmissivities are usually related to the interface heat conductance G and properties of materials 1 and 2 via the model [22, 31, 32]

$$G = \frac{1}{2 \left[2 \left(\int_{\omega} T_{12,\omega} C_{\omega,1} v_{\omega,1} d\omega \right)^{-1} - \left(\int_{\omega} C_{\omega,1} v_{\omega,1} d\omega \right)^{-1} - \left(\int_{\omega} C_{\omega,2} v_{\omega,2} d\omega \right)^{-1} \right]}. \quad (7)$$

2.2 Inverse problem formulation

Our goal is to obtain an accurate and reliable approximation to the function τ_ω from the experimental measurements of the temperature profiles. The free path distribution can be subsequently obtained via equation (5), assuming that the group velocities v_ω are known [19]. We formulate the reconstruction as an extended form of the optimization problem first proposed in [19], in which τ_ω and $T_{12,\omega}$ are determined as the functions that minimize the discrepancy between the experimental measurements and

the BTE solutions. Relaxation times in the optimization formulation are represented by τ_ω^S , where ω is the frequency and S is the branch which can be longitudinal/transverse acoustic/optical. Here, $S \in \{LA, TA_1, TA_2\}$, where LA denotes the longitudinal acoustic branch, while TA_1 and TA_2 represent the two transverse acoustic branches. Optical phonons are not considered here, due to their small contribution to transient heat transport [33]; if desired, they can be added as an additional unknown branch (see discussion in [19]).

Following the previously proposed functional form for the relaxation times [19], we represent τ_ω^S as a piecewise linear relation between $\log(\tau_\omega^S)$ and $\log(\omega)$, smoothed via third order polynomial functions (of $\log(\omega)$)

$$\begin{aligned} \log(\tau_\omega^S) = & \\ & \sum_{j=0}^{M-1} \left[\frac{\log(\tau_{\omega_{j+1}}^S) - \log(\tau_{\omega_j}^S)}{\log(\omega_{j+1}^S) - \log(\omega_j^S)} (\log(\omega) - \log(\omega_j^S)) + \log(\tau_{\omega_j}^S) \right] \mathbb{1}_{\omega \in [X_{2j}^S, X_{2j+1}^S]} + \\ & \sum_{j=1}^{M-1} \left[a_j^S [\log(\omega)]^3 + b_j^S [\log(\omega)]^2 + c_j^S \log(\omega) + d_j^S \right] \mathbb{1}_{\omega \in (X_{2j-1}^S, X_{2j}^S)}, \quad (8) \end{aligned}$$

where M determines the number of segments. There are $2M$ unknowns in the relaxation time model for each branch $S \in \{LA, TA_1, TA_2\}$, consisting of $\omega_1^S, \dots, \omega_{M-1}^S$, and $\log(\tau_{\omega_0}^S), \dots, \log(\tau_{\omega_M}^S)$, since the minimum and maximum frequencies for each branch (ω_0^S and ω_M^S) are known (input). Also, $\mathbb{1}_{\omega \in \mathcal{S}}$ denotes the indicator function whose value is 1 if $\omega \in \mathcal{S}$, and 0 if $\omega \notin \mathcal{S}$. The parameters X_j^S , a_j^S , b_j^S , c_j^S , and d_j^S have the same meaning as in [19]; their definition can also be found in Appendix A.

The interface transmissivity as a function of frequency $T_{12,\omega}^S(\omega)$ is also expressed using piecewise linear relations. This function is additionally constrained to vary between 0 and $\min\{1, \frac{v_{\omega,2}C_{\omega,2}}{v_{\omega,1}C_{\omega,1}}\}$ since transmissivity represents a probability. Note that the upper bound is set by both the maximum permissible probability of $T_{12,\omega}$ and $T_{21,\omega}$; the latter is determined via (6). The specific functional form is given by

$$\begin{aligned} T_{12,\omega}^S = \max \left\{ \min \left\{ \sum_{j=0}^{\bar{M}-1} \left[\frac{T_{12,\bar{\omega}_{j+1}}^S - T_{12,\bar{\omega}_j}^S}{\bar{\omega}_{j+1}^S - \bar{\omega}_j^S} (\omega - \bar{\omega}_j^S) + T_{12,\bar{\omega}_j}^S \right] \mathbb{1}_{\omega \in [\bar{X}_{2j}^S, \bar{X}_{2j+1}^S]} + \right. \right. \\ \left. \left. \sum_{j=1}^{\bar{M}-1} [\bar{a}_j^S \omega^3 + \bar{b}_j^S \omega^2 + \bar{c}_j^S \omega + \bar{d}_j^S] \mathbb{1}_{\omega \in (\bar{X}_{2j-1}^S, \bar{X}_{2j}^S)}, \frac{v_{\omega,2}C_{\omega,2}}{v_{\omega,1}C_{\omega,1}}, 1 \right\}, 0 \right\}. \quad (9) \end{aligned}$$

The role of the parameters \bar{M} , $\bar{\omega}_j^S$, \bar{X}_j^S , \bar{a}_j^S , \bar{b}_j^S , \bar{c}_j^S , and \bar{d}_j^S is similar to M , ω_j^S , X_j^S , a_j^S , b_j^S , c_j^S , and d_j^S in equation (8), respectively; definitions can be found in Appendix B. In the remainder of the paper, we will use the compact vectorial notations $\boldsymbol{\tau}^S = (\tau_{\omega_0}^S, \dots, \tau_{\omega_M}^S)$, $\boldsymbol{\omega}^S = (\omega_1^S, \dots, \omega_{M-1}^S)$, $\mathbf{T}_{12}^S = (T_{12,\bar{\omega}_0}^S, \dots, T_{12,\bar{\omega}_{\bar{M}}}^S)$, and

$\bar{\omega}^S = (\bar{\omega}_1^S, \dots, \bar{\omega}_{M-1}^S)$ to represent the unknown parameters. Similarly, the vector of all unknowns is

$$\mathbf{U} = (\boldsymbol{\tau}^{LA}, \boldsymbol{\tau}^{TA_1}, \boldsymbol{\tau}^{TA_2}, \boldsymbol{\omega}^{LA}, \boldsymbol{\omega}^{TA_1}, \boldsymbol{\omega}^{TA_2}, \mathbf{T}_{12}^{LA}, \mathbf{T}_{12}^{TA_1}, \mathbf{T}_{12}^{TA_2}, \bar{\omega}^{LA}, \bar{\omega}^{TA_1}, \bar{\omega}^{TA_2}). \quad (10)$$

Here we note that this formulation does not use any of the previously proposed interface transmissivity models, such as the diffuse mismatch model (DMM) and the acoustic mismatch model (AMM) [26, 34], which are known to be inaccurate, in particular at higher temperatures [35]. Note that we have used the DMM model in section 4 for generation of synthetic experimental data (for validation purposes), but that in no way implies an assumption of such behavior during the reconstruction process.

Assuming, without loss of generality, that we are interested in reconstructing the relaxation times of material 1, the objective function that needs to be minimized is

$$\mathcal{L} = \min_{\mathbf{U}} \left[\frac{\sum_{t, \mathbf{x}, L} |T_m(t, \mathbf{x}; L) - T_{\text{BTE}}(t, \mathbf{x}; L, \mathbf{U})|}{N} + \alpha \left| 1 - \frac{1}{3\kappa_1} \int_{\omega} C_{\omega,1} \tau_{\omega,1}(\mathbf{U}) v_{\omega,1}^2 d\omega \right| + \beta \left| 1 - \frac{1}{2G \left[2 \left(\int_{\omega} T_{12,\omega}(\mathbf{U}) C_{\omega,1} v_{\omega,1} d\omega \right)^{-1} - \left(\int_{\omega} C_{\omega,1} v_{\omega,1} d\omega \right)^{-1} - \left(\int_{\omega} C_{\omega,2} v_{\omega,2} d\omega \right)^{-1} \right]} \right| \right], \quad (11)$$

where $T_m(t, \mathbf{x}; L)$ is the experimentally measured temperature, T_{BTE} is the temperature obtained from solution of the BTE (the same temperature in equation (4)), N is the total number of (independent) measurements available with $\sum_{t, \mathbf{x}, L} 1 = N$, and L is the different length scales at which the data for relaxation profiles are available.

The second and third terms in the definition of \mathcal{L} are regularizers whose purpose is to improve the quality of the optimization process. The second term uses the (presumed known) value of the heat conductivity of material 1, κ_1 , to improve the quality of the reconstructed relaxation times, while the third term uses the (presumed known) value of the interface thermal conductance, G , to enhance the accuracy of the reconstruction. We have empirically determined that setting $0.01 < \alpha, \beta < 1$ improves the reconstruction considerably. If the value of κ_1 and/or G is unknown, the respective terms can be removed (by setting the corresponding coefficient to zero). As stated previously, in the present work we have assumed that G is unknown, therefore, the objective function used for reconstruction/validation purposes in the remainder of the paper only features the first and the second terms ($\beta = 0$).

3 Reconstruction

As in our previous work, the reconstruction is based on an optimization process utilizing the Nelder-Mead (NM) algorithm [36]. A detailed description of the algorithm and typical parameter values can be found in [19].

Reconstruction proceeds by comparing solutions of equation (1), obtained via adjoint MC simulations [25] using \mathcal{N}_{BTE} particles, with the counterpart N measurements of T_{m} . As discussed before, phonon group velocities were assumed known, while τ_{ω} was described by the model given in equation (8) with $M = 3$ (a piecewise linear function with three segments) and $T_{12,\omega}$ by the model described by equation (9) with $\bar{M} = 1$. We have considered three branches for relaxation times (representing three acoustic branches), leading to $3 \times 6 = 18$ unknowns and only one branch for the transmissivities, adding two unknowns, leading to a total of 20 unknowns. We have observed that increasing the number of branches and/or the value of \bar{M} does not affect the quality of the reconstructed relaxation times significantly, implying that the reconstruction is less sensitive to the values of $T_{12,\omega}$ (see the discussion in section 4.3).

In order to increase the probability of finding the global minimum of the objective function (11), we have used a process referred to as “graduated optimization”. In this process, the optimization of a non-convex function is performed in multiple stages by breaking down the problem into a series of consecutive (simpler) sub-problems, whose initial condition is the optimized value of the previous stage [37].

Previously, we have proposed a reconstruction algorithm [19] which featured four stages of optimization. Here, in the presence of an interface, we have found that an additional stage is helpful. This additional stage, that we refer to as stage zero, provides an initial estimate for the parameters of the interface transmissivity function, $T_{12,\omega}$, that is needed in stage one. If the value of G is known, this stage is not required.

3.1 Problems with known interface conductance

Since the role of stage zero is better understood in the context of the first stage of the optimization process, we first discuss stages one through four, suitable for problems with known G ; stage zero is discussed in the following subsection.

In the first stage, we assume that all relaxation times (three branches) are described by one line (one branch with $M = 1$), leading to two unknowns, namely τ_{ω_0} and τ_{ω_1} . We also use one line to describe the unknown transmissivities, contributing two additional unknowns, namely $T_{12,\bar{\omega}_0}$ and $T_{12,\bar{\omega}_1}$. For $M = 1$ and $\bar{M} = 1$, equations (8) and (9) reduce to

$$\log(\tau_{\omega}) = p \log(\omega) + k, \quad (12)$$

and

$$T_{12,\omega} = \hat{p}\omega + \hat{k}, \quad (13)$$

respectively, where the superscript S is omitted since in this stage all branches obey the same model. We also note that the parameters in (8) are related to p and k via

$$\tau_{\omega_0} = \omega_0^p 10^k, \quad \tau_{\omega_1} = \omega_1^p 10^k, \quad (14)$$

while the parameters in (9) are related to \hat{p} and \hat{k} via

$$T_{12,\bar{\omega}_0} = \hat{p}\bar{\omega}_0 + \hat{k}, \quad T_{12,\bar{\omega}_1} = \hat{p}\bar{\omega}_1 + \hat{k}. \quad (15)$$

In order for the values of p and k to satisfy the given value of κ (heat conductivity of the material under study; κ_1 in equation (11)), we must have

$$k = \log \left(\frac{3\kappa}{\int_{\omega} C_{\omega} \omega^p v_{\omega}^2 d\omega} \right), \quad (16)$$

where $C_{\omega} = C_{\omega,1}$ and $v_{\omega} = v_{\omega,1}$. Similarly, with the value of G known, the following relation should hold between \hat{p} and \hat{k}

$$\hat{k} = \frac{2}{1 + \frac{\int_{\omega} C_{\omega,1} v_{\omega,1} d\omega}{2G} + \frac{\int_{\omega} C_{\omega,1} v_{\omega,1} d\omega}{\int_{\omega} C_{\omega,2} v_{\omega,2} d\omega}} - \hat{p} \frac{\int_{\omega} C_{\omega,1} v_{\omega,1} \omega d\omega}{\int_{\omega} C_{\omega,1} v_{\omega,1} d\omega}. \quad (17)$$

Equations (16)-(17) provide relationships between two first-stage unknown variables and known material properties. While the first stage features four unknowns (k , \hat{k} , p , \hat{p}), due to these relations, only two parameters (p and \hat{p}) need to be guessed as part of the initialization. Once the parameters p and \hat{p} are specified, k and \hat{k} can be determined via equations (16) and (17), from which the initial condition for τ_{ω} and $T_{12,\omega}$ can be calculated using equations (14) and (15). Note that this treatment does not change the number of unknown parameters in stage one; instead, it increases the efficiency of the optimization algorithm by dismissing initial conditions that are inconsistent with the material/interface properties.

In the second stage, the LA and TA modes of the relaxation time function are still assumed to be the same but the intended number of segments is used, increasing the number of unknowns for the relaxation times to $2M$ (six in the present case). The number of unknowns for the transmissivity function stays at two, leading to a total of 8 unknowns. The initial condition for this stage is taken to be the same as the optimized value of the previous stage (or a slightly perturbed version).

In the third stage, we repeat the optimization process, now for $4M$ unknowns (the two TA branches are assumed to be the same, $\tau_{\omega}^{TA1} = \tau_{\omega}^{TA2}$), starting from the optimized parameters of the second stage. The number of unknowns for the transmissivity function does not change at this stage. Therefore, the total number of unknowns is $12 + 2 = 14$.

Finally, we perform the optimization for all $6M$ unknowns of the relaxation times and the two unknowns of the transmissivity function (total of $6M + 2 = 20$ unknowns), starting from the optimized parameters of the previous stage. The optimized values at this stage are the final values parameterizing the relaxation time and transmissivity functions.

3.2 Problems with unknown interface conductance

As explained in the previous section, if G is known, given a guess for \hat{p} , \hat{k} can be calculated using equation (17). If, however, G is unknown, (17) cannot be used. Therefore, an additional stage—stage zero—is added to the optimization process to provide an initial value for \hat{k} that is consistent with the initial guess for \hat{p} to be used in stage one.

To obtain a value for \hat{k} consistent with the value of \hat{p} to be used in stage one we perform an optimization assuming constant relaxation times ($\tau(\omega) = \tau$) and a fixed value of \hat{p} . Since the single constant (gray) relaxation time is related to the (assumed known) thermal conductivity via

$$\tau = \frac{3\kappa}{\int_{\omega} C_{\omega} v_{\omega}^2 d\omega}, \quad (18)$$

\hat{k} is the only unknown function at this stage and can be solved for by optimization. Using this optimized value and the guess for \hat{p} , initial conditions for stage one for $T_{12, \bar{\omega}_0}$ and $T_{12, \bar{\omega}_1}$ can be obtained from (15).

The initial guesses for stage one for τ_{ω_0} and τ_{ω_1} remain the same as in the case of known G , namely,

$$\tau_{\omega_0} = \frac{3\kappa\omega_0^p}{\int_{\omega} C_{\omega}\omega^p v_{\omega}^2 d\omega}, \quad \tau_{\omega_1} = \frac{3\kappa\omega_1^p}{\int_{\omega} C_{\omega}\omega^p v_{\omega}^2 d\omega} \quad (19)$$

(see equations (14) and (16)).

3.3 Initialization protocol

To reduce the probability of the reconstruction being trapped in a local minimum, in our approach, we repeated the first stage of the optimization for four different values of p and four different values of \hat{p} , leading to a total of $4 \times 4 = 16$ distinct initial conditions. Consequently, since \hat{k} for a given \hat{p} is determined via the zeroth stage, the zeroth stage was also repeated four times. The second stage was also repeated for five different initial conditions which were the five lowest values of \mathcal{L} obtained from optimizations in stage one¹. Finally, third and fourth stages were performed for only one initial condition corresponding to the lowest value of \mathcal{L} in the second and third stages of the optimization, respectively.

To reduce cost, MC simulations during the zeroth, first and second stages of the optimization process used $\mathcal{N}_{\text{BTE}} = 10^4$ particles for calculation of T_{BTE} . During the third and fourth stages of the process, since we were looking for more accurate solutions, the number of particles was increased to $\mathcal{N}_{\text{BTE}} = 10^6$. Since the computational time for each adjoint MC simulation is proportional to \mathcal{N}_{BTE} [25], given our choices for \mathcal{N}_{BTE} , the cost of the first three stages of the optimization is negligible compared to the cost of the last two stages, therefore, repeating them a number of times starting from different initial conditions does not increase the cost of the reconstruction process significantly.

¹In some cases where multiple simulations of stage one had similar values for \mathcal{L} , we repeated simulations of stage two for all such initial conditions, leading to more than five simulations in the second stage.

4 Validation

We demonstrate the use and validate the effectiveness and accuracy of the proposed methodology using synthetic data obtained from MC simulations of equation (1) for the 2D-dots problem [7], using the adjoint deviational formulation described in [25]. In other words, we generate “synthetic” experimental data $T_m(t, \mathbf{x}; L)$ by solving equation (1) for a particular material model and then use the proposed formulation to reconstruct the material properties (relaxation times and free path distribution) and compare with the input data. Synthetic data are preferable (to experimental data) because they allow us to validate the accuracy of the algorithm directly with no need to account for possible experimental error, as well as modeling error resulting from neglecting various effects (e.g. electronic transport) present in experiments. A sketch of the 2D-dots geometry can be found in figure 1.

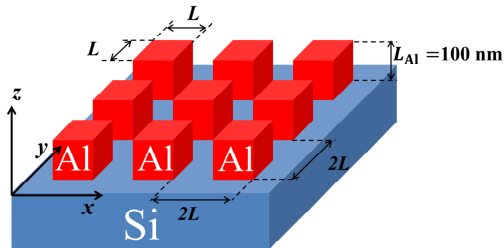


Figure 1: 2D-dots geometry, comprising a periodic array of Al “dots” on a Si substrate. The structure is assumed to be sufficiently large that it can be approximated as infinite in the x and y directions; moreover, the Si substrate thickness is sufficiently large to be approximated as semi-infinite. The dot height is constant at $L_{\text{Al}} = 100$ nm, while the dot base is square with edge length L . The ratio between L and the periodicity of the structure is constant at 0.5. The experimental measurement, $T_m(t, \mathbf{x}; L)$, corresponds to the surface temperature of Al after the initial heating event at $t = 0$.

4.1 Generation of synthetic experimental data

The material under study is taken to be silicon. We have considered two different sets of silicon material properties similar to the data we have used previously [19]. The first model considered (thermal conductivity $\kappa = 139.7 \text{ Wm}^{-1}\text{K}^{-1}$) is described in [21, 38] and will be referred to as the *ab initio* model throughout this paper. The second model considered here is described in [22, 32] (thermal conductivity $\kappa = 143.8 \text{ Wm}^{-1}\text{K}^{-1}$) and will be referred to as the *Holland* model. Also for Al, we used the material model adapted from the dispersion relation in [39] with constant relaxation time of $\tau_{\text{Al}} = 10$ ps as in [22, 32].

Synthetic data was generated using two different interface models. The first model is the DMM which is widely used in transport theory [26]. According to this model, the

transmissivity from material 1 to 2 is given by

$$T_{12,\omega} = \frac{C_{\omega,2}v_{\omega,2}}{C_{\omega,1}v_{\omega,1} + C_{\omega,2}v_{\omega,2}}. \quad (20)$$

The second model is based on experimental measurements shown in figure 12 of [35]; it will be referred to as the “experimental” model in the present work.

The generated synthetic temperature relaxation profiles are in the form of $T_m(0 \leq t \leq 5 \text{ ns}, \mathbf{x}_s; L)$, implying measurement at the surface of Al, $\mathbf{x}_s = (x, y, 100 \text{ nm})$ (based on the coordinates in figure 1) for 5 ns, which is a typical measurement time in pump-probe experiment of the 2D-dots geometry [7]. Ten different side lengths were simulated; namely, $L = 10 \text{ nm}, 20 \text{ nm}, 40 \text{ nm}, 100 \text{ nm}, 500 \text{ nm}, 750 \text{ nm}, 1 \mu\text{m}, 2.5 \mu\text{m}, 5 \mu\text{m}$, and $50 \mu\text{m}$. Each simulation is sampled at 100 discrete time instances (during the relaxation). As a result, 1000 total T_m measurements were available for reconstruction ($N = 1000$). The data were generated using both essentially noise-free MC simulations via $\mathcal{N}_m = 10^8$ particles (\mathcal{N}_m is the number of particles used in the MC simulations for *generating synthetic “experimental” data*), and noisy MC simulations with $\mathcal{N}_m = 10^3$ particles. The latter were used to assess the method performance in the presence of noisy experimental measurements (see figure 5 of [19] for a comparison of the noisy and noise-free temperature profiles). The noisy synthetic data have been observed to have a standard deviation of 0.02 K. This standard deviation makes the uncertainty in T_m significantly larger than the noise in common experimental data (e.g. compare the noisy temperature profile of figure 5 of [19] with figure 2c of [7]).

4.2 Results

In this section, we present comparisons between the reconstructed relaxation times $\tau_\omega = \tau(\omega)$ (and associated cumulative distribution function (CDF) of free paths) and the corresponding properties used as input for generating the synthetic experimental data. The CDF is defined as $F(\Lambda) = \frac{1}{3\kappa} \int_{\omega^*(\Lambda)} C_\omega v_\omega^2 \tau_\omega d\omega$, where $\omega^*(\Lambda)$ is the set of modes such that $\Lambda_\omega \leq \Lambda$, that is $\omega^*(\Lambda) = \{\omega | \Lambda_\omega \leq \Lambda\}$; the corresponding probability density function (of free paths) is given by $f = \frac{dF}{d\Lambda}$.

Our comparison figures also display the reconstructed interface transmissivities, although, as stated previously, the goal of the algorithm and the present paper is not to specifically determine the mode dependent transmissivities; the latter are a by-product of the relaxation-time reconstruction. In these figures, the input material properties (which synthetic relaxation profiles are generated from) are labeled as “true”, while the reconstructed properties (obtained through the optimization process) are labeled as “reconstructed”. The reconstructed results are provided in sections 4.2.1 and 4.2.2.

4.2.1 Ab initio model

In this section, we present the reconstructed silicon material properties for the ab initio material model. This model has two TA branches, therefore, there is a total of $6M + 2\bar{M} = 20$ unknowns.

Figures 2 and 3 show a comparison between the true material parameters and the reconstructed ones for the ab initio silicon material properties using the experimental interface transmissivities, in the absence and presence of noise, respectively. We observe that the reconstructed relaxation times are close to the true data. We also note that the discrepancy is more noticeable for low frequencies, primarily due to the low density of states of these frequency ranges; in particular, the density of states of the LA modes for $\omega \leq 8 \times 10^{12}$ rad/s is zero (i.e. none of the terms in (11) influences τ_{ω}^{LA} for $\omega \leq 8 \times 10^{12}$ rad/s). These figures show that the error in the reconstructed transmissivities is more significant. However, the final value of the objective function is small, indicating that accurate reconstruction of relaxation times distribution that can reproduce the input temperature profiles (comparisons between input temperature profiles and their counterparts predicted by the reconstructed properties can be found in figure 8) are possible even if the transmissivities are not accurately reconstructed.

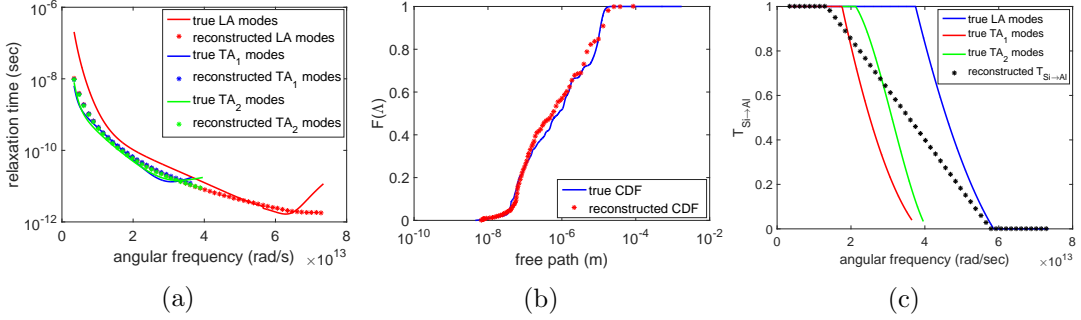


Figure 2: Reconstructed material properties with ab initio relaxation times, experimental transmissivities, and noise-free synthetic relaxation profiles.

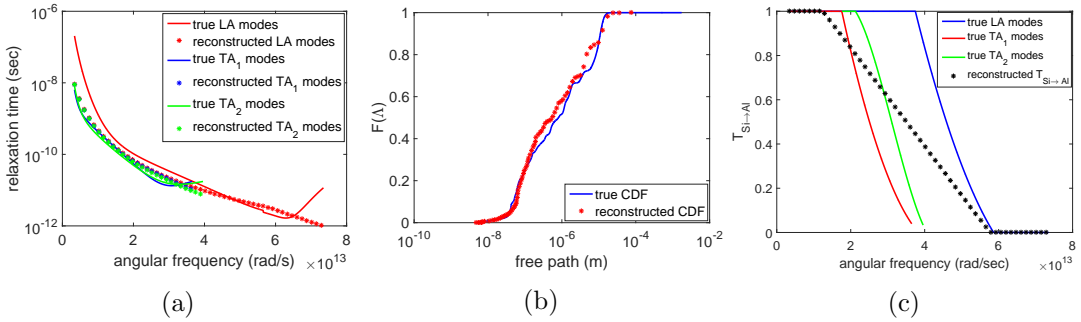


Figure 3: Reconstructed material properties with ab initio relaxation times, experimental transmissivities, and noisy synthetic relaxation profiles.

4.2.2 Holland model

In this section, we present results for the Holland material model. This model assumes that the two TA branches are the same and as a result, the optimization process consists of three stages (plus the stage zero) with a total of $4M + 2\bar{M} = 14$ unknowns.

Figures 4 and 5 show a comparison between the true material parameters and the reconstructed ones for the Holland set of data using the experimental and DMM interface transmissivities, respectively, in the absence of noise. We observe that the algorithm is able to capture true relaxation times with reasonable accuracy. Our conclusions are similar to the case of ab-initio data, namely, even though the transmissivities are not reproduced accurately, the relaxation times, which are the quantities of interest, are accurately reconstructed. We have also observed (not shown here) that the same conclusion can be made in the case of noisy data.

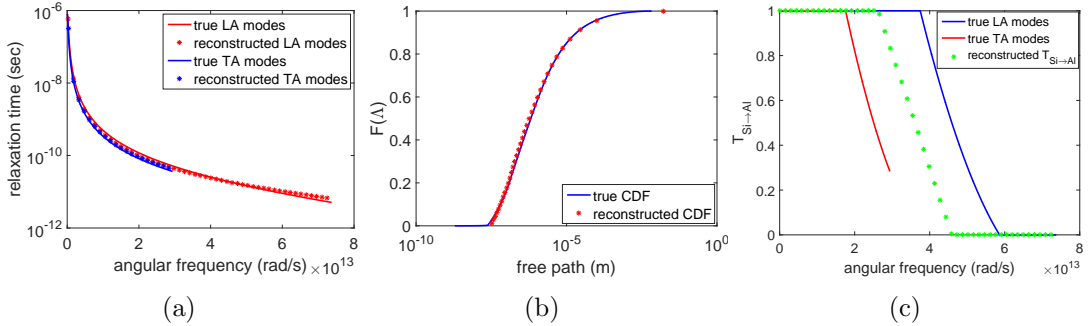


Figure 4: Reconstructed material properties with Holland relaxation times, experimental transmissivities, and noise-free synthetic relaxation profiles.

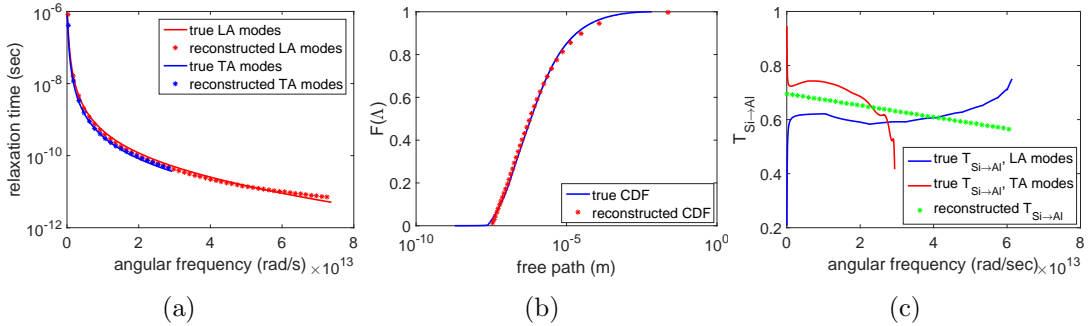


Figure 5: Reconstructed material properties with Holland relaxation times, DMM transmissivities, and noise-free synthetic relaxation profiles.

4.3 Effect of interface treatment

In the previous sections we have observed that one line ($\bar{M} = 1$) results in a sufficiently adequate representation of the transmissivity (for all branches) *for the relaxation times to be reconstructed accurately*. Given the accurate reconstruction of the relaxation times and temperature fields (see figures 8a and 8b below), we would expect the interface properties to be captured correctly at least in an “average” sense. Indeed, in the above comparison figures (2-5) we observe that although the reconstructed transmissivity profiles are not very accurate in a spectral sense, they do capture the interface transmissivity in an average sense. To make this observation more quantitative, we have calculated the interface thermal conductance G associated with each of the reconstructed transmissivities in sections 4.2.1 and 4.2.2. The resulting values, calculated using equation (7), are provided in table 1, which shows that the interface thermal conductances are, generally speaking, close to the thermal conductance associated with the true data from which the synthetic temperature relaxation profiles are generated. In other words, these results suggest that reconstruction of the relaxation times is only sensitive to the aggregate effect of the interface, as captured, for example, by a simple linear (as function of frequency) model.

Silicon model/ interface model/ data type	Holland exp. noise-free	Holland DMM noise-free	Holland exp. noisy	Holland DMM noisy	Ab initio exp. noise-free	Ab initio exp. noisy
G (MW/m ² K)	260	367	260	367	567	567
Reconstructed G (MW/m ² K)	265	353	273	364	630	658

Table 1: Calculated interface heat conductance based on the true (first row) and reconstructed (second row) interface transmissivities; “exp.” denotes the experimental interface model adapted from [35].

To verify this assertion, we have performed the optimization using a more complex parameterization in equation (9) where different branches are represented by different distinct linear functions, for all different cases of section 4.2. An example of such reconstruction is provided in figure 6 for the Holland material model, experimental transmissivity, and noise-free synthetic data. We observe that the quality of the reconstruction has not improved compared to figure 4. Accordingly, we have not noticed any significant improvement in the final value of the objective function.

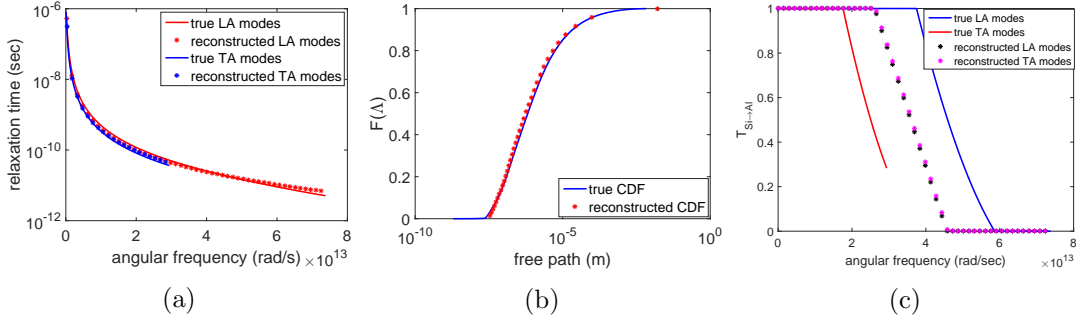


Figure 6: Reconstructed material properties with Holland relaxation times, experimental transmissivities, and noise-free synthetic relaxation profiles with separate linear models for frequency-dependent transmissivities of LA and TA branches.

As a further consistency check, we have repeated one of the reconstruction tests of section 4.2.2 assuming $T_{21,\omega}$ (the transmissivity from Al to Si) to be the unknown (and hence constrained to be linear in angular frequency) function. The result for the experimental transmissivity and noise-free synthetic data is provided in figure 7. As expected, the reconstructed $T_{12,\omega}$ transmissivities (obtained by applying principle of detailed balance to reconstructed $T_{21,\omega}$) for the different branches are not the same as before and they are now distinct for different branches. However, comparison with figure 4 suggests that this result serves as the best, perhaps, illustration of our previous conclusion, namely that the reconstruction is fairly insensitive to the complexity of the parameterization used for the interface (provided it is reasonable); despite the clearly different results for $T_{12,\omega}$, the maximum discrepancy between the two reconstruction results (for the relaxation times) is only 0.7%, implying that they are essentially identical. The value of interface conductance associated with this reconstruction is $G = 273$ MW/m²K, which is very close to the heat conductance of the reconstruction of figure 4 ($G = 265$ MW/m²K from table 1).

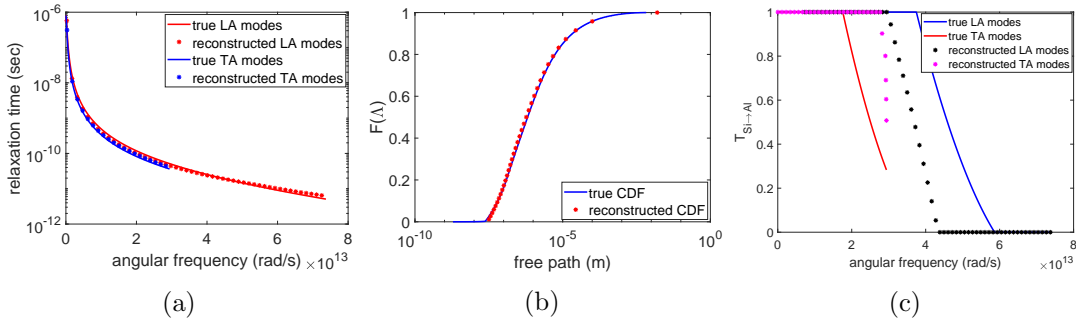


Figure 7: Reconstructed material properties with Holland relaxation times, experimental transmissivities, and noise-free synthetic relaxation profiles with $T_{21,\omega}$ (the transmissivity from Al to Si) being unknown.

Figure 8 compares the synthetic input temperature profiles with relaxation profiles generated from reconstructed properties for some of the cases considered in this section. All plots show negligible differences between the input and reconstructed temperature profiles; the same conclusion is reached by observing the very small final value of \mathcal{L} . The trend for other reconstruction results (not shown here) is the same. This figure also confirms our earlier claim that the free time reconstruction can proceed without precise knowledge of the transmissivity profiles, making the present reconstructions (using simple models for the transmissivity) feasible.

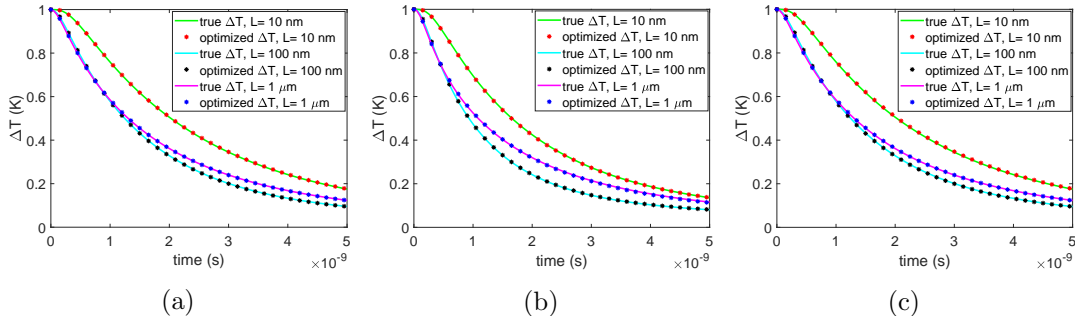


Figure 8: Comparison between the synthetic temperature profiles and the ones generated from the reconstructed properties of (a)- figure 4, (b)- figure 2, and (c)- figure 7.

4.4 Why is interface transmissivity reconstruction not as accurate as relaxation time reconstruction?

So far, we have empirically shown that accurate reconstruction of the relaxation times does not require reconstruction of the interface transmissivities to the same accuracy level; specifically, our results suggest that treating the transmissivities using a simple linear model (as a function of frequency) for all branches is sufficient. At the same time, increasing the model complexity does not improve the quality of the interface property reconstruction, suggesting that it is, perhaps, not possible to obtain accurate transmissivity reconstructions from the TDTR setup we have considered here.

In order to gain some further insight we have performed reconstructions for different dot properties and heights. Figure 9 shows the reconstruction result which uses the Holland model for Si, experimental transmissivities, noise-free data, and $\tau'_{\text{Al}} = 100\tau_{\text{Al}} = 1$ ns. This leads to an average Kn number inside the Al of 17 (based on the dot height), with a range of 17-170 (the characteristic length scale is taken to be the smallest of the dot height, L_{Al} , and L). We observe that, similar to all reconstructions of sections 4.2-4.3, even though the transmissivities are only approximately reconstructed, the relaxation times are reconstructed accurately. We have also performed reconstructions for other Al relaxation times ($\tau_{\text{Al}} = 100$ ps), other Si properties (ab initio data), and other interface properties (DMM) as well as different dot heights ($L_{\text{Al}} = 10$ nm, 25 nm, and 50 nm); the conclusion is essentially the same in all cases.

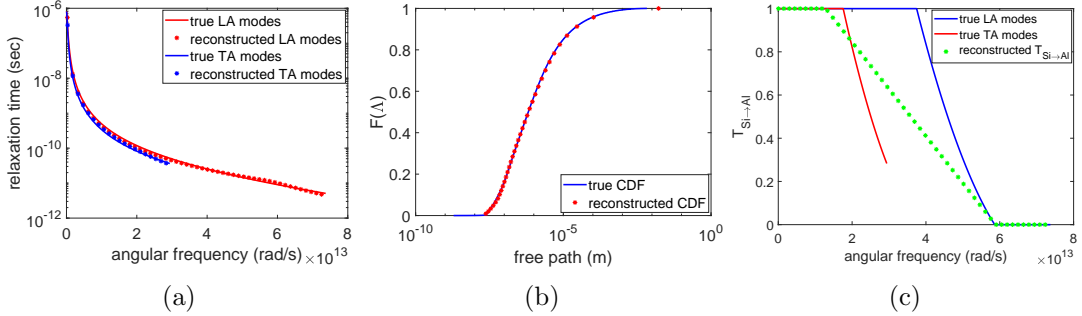


Figure 9: Reconstructed material properties with Holland relaxation times, experimental transmissivities, and noise-free temperature profiles with $\tau_{Al}^I = 100\tau_{Al} = 1$ ns.

An important observation stemming from these numerical experiments is that the reconstructed transmissivity profile in figure 9 is different from the one shown in figure 4. At the same time, as observed before in table 1 for other reconstructions, G is approximately correctly reconstructed ($G = 249$ MW/m²K). Although not surprising given our previous findings and discussion, the different transmissivity profile observed here is attributed to the fact that the transport regime (aluminum Knudsen number based on dot height) in the aluminum is different, altering the relative importance of different parts of the frequency spectrum (see [40] for a discussion). The correctly reconstructed value of G , on the other hand, suggests that temperature relaxation data at a fixed aluminum dot height, provides only sufficient information for a reconstruction of some “aggregate” effect of the interface. This may be attributed to the fact that the dot height has a more direct effect on the phonon population crossing the interface than length scale L .

In summary, what separates relaxation times from interface transmissivities in the present context is that TDTR experiments sample a variety of transport regimes in the substrate material (by varying the characteristic values of length scale L), while only sampling one regime as far as the interface is concerned. As a result, relaxation times are accurately reconstructed, while interface properties are only approximately reconstructed (only reconstructed in an aggregate sense). The decoupling of these two unknowns, possibly due to the fact that they correspond to two distinct parts of the system (bulk vs boundary), has a profound effect on the feasibility of the reconstruction of the relaxation times, which is the objective of this work. Implications of this observation for the reconstruction of interface properties are discussed in section 5.

4.5 Comparison to the effective thermal conductivity approach

In this section, we compare our approach with the prevalent reconstruction approach, namely the method based on the effective thermal conductivity.

The effective heat conductivity approach aims at reconstructing the phonon free path distribution directly from the measured temperature relaxation profiles, assuming

that in the non-diffusive regime, heat transport can still be represented using the Fourier heat conduction equation with a suppressed heat conductivity, $\kappa_{\text{eff}} \leq \kappa$ [6]. The effective heat conductivity approach is based on the *approximation*

$$\frac{\kappa_i}{\kappa} = \int_0^\infty S(\chi_i) f(\Lambda_\omega) d\Lambda_\omega = \int_0^\infty -\frac{dS(\chi_i)}{d\chi_i} \frac{d\chi_i}{d\Lambda_\omega} F(\Lambda_\omega) d\Lambda_\omega, \quad (21)$$

where κ_i is the effective heat conductivity associated with L_i , obtained by fitting the response $T_m(t, \mathbf{x}; L_i)$ to the solution of Fourier heat conduction equation with κ_i treated as the unknown in the fitting process. In the above equation, χ_i is a dimensionless quantity relating length scale to free paths, here taken to be $\chi_i = \Lambda_\omega / L_i$, $S(\chi_i)$ is the suppression function, and $f(\Lambda_\omega)$ and $F(\Lambda_\omega)$ are defined at the beginning of section 4.2.

While the approximate suppression function $S(\chi_i)$ can be obtained analytically under a set of rather restrictive assumptions [19] for a few simple geometries such as 1D TTG [6], for most geometries, including 2D-dots, no analytical expression is available. Putting aside the fact that such a function may not exist, in such cases, it has been proposed [21] that it can be approximated by the suppressed effective thermal conductivity of the gray model in the same geometry, namely $S(\chi_i) = \kappa_g(\chi_i) / \kappa$, where the subscript g denotes gray model and $\kappa_g(\chi_i)$ denotes the effective thermal conductivity measured by fitting the relaxation profile to the heat conduction equation solution in the said geometry. Provided with measurements of length scale dependent effective heat conductivities, κ_i , $F(\Lambda_\omega)$ can be obtained by solving the inverse problem in equation (21) using a convex optimization framework [6].

In order to compare with our results, we performed the above procedure for the Holland model of silicon with both the experimental and DMM transmissivity functions and noise-free synthetic temperature profiles. The suppression function used for the reconstruction along with its derivative based on the experimental transmissivity are plotted in figure 10a. The suppression function was calculated by fitting a polynomial to ten different values of $\kappa_g(\chi_i) / \kappa$, obtained from gray simulations with $L = 100$ nm by varying the gray mean free path. The suppression function with DMM transmissivities is essentially the same. Figure 10b shows $\kappa_{\text{eff}}(L)$ (κ_i in equation (21)) normalized by κ , as obtained by MC simulations of ten different domain length scales (L) based on both experimental and DMM transmissivities. Finally, figure 10c plots the reconstructed free path distribution, obtained using the convex optimization problem formulated in [6] with the same values for the number of integration points and parameter η (see [6] for more details), for both interface models. Our results do not change significantly if we use more than ten data points.

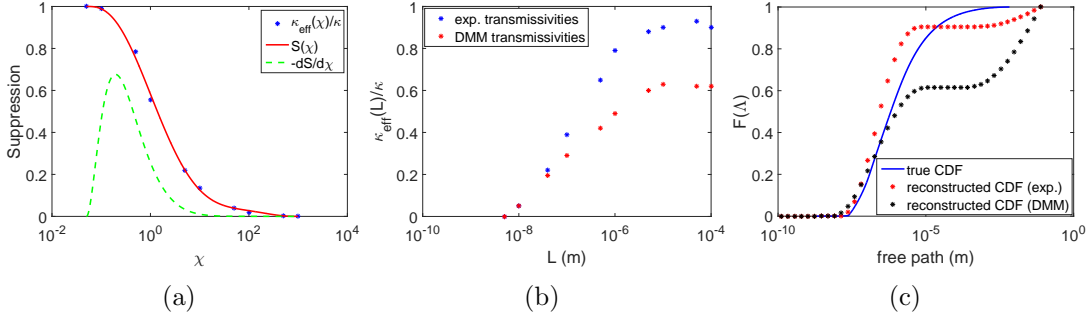


Figure 10: Reconstructed free path distribution based on effective thermal conductivity approach (c); “exp.” denotes the experimental interface model adapted from [35]. Length dependent cumulative effective heat conductivity (b). The suppression function based on experimental transmissivity interface model (a).

Three different types of discrepancies can be detected in figure 10c. The first discrepancy is the mismatch with the true CDF in the $\Lambda \lesssim 5 \mu\text{m}$ region for both models which can be attributed to the gray approximation used for the calculation of the suppression function; a similar trend has been observed previously in [21]. The second type of discrepancy is the mismatch with the true CDF, and in particular the plateau in F , in the range $5 \mu\text{m} \lesssim \Lambda \lesssim 1 \text{mm}$ in both models. Although constraining the CDF to reach 1 at large free paths (a property of the cumulative distribution function) has forced the CDF to eventually do so around $\Lambda = 5 \text{cm}$, saturation of $\kappa_{\text{eff}}(L)/\kappa$ for $L \gtrsim 5 \mu\text{m}$ (see figure 10b) has caused significant discrepancy between the reconstructed and true free path distribution in the region $5 \mu\text{m} \lesssim \Lambda \lesssim 1 \text{mm}$. The third discrepancy is the significantly different plateau value for F for the two different interface models, which can be directly traced to the significantly different values at which $\kappa_{\text{eff}}/\kappa$ saturates for $L \gtrsim 5 \mu\text{m}$ for the two models.

It is very important to note that the saturation of $\kappa_{\text{eff}}(L)/\kappa$ for $L \gtrsim 5 \mu\text{m}$ is a result of the transport regime in silicon never becoming fully diffusive, even at $L = 1 \text{mm}$. Since the reconstruction critically depends on the value of the ratio $\kappa_{\text{eff}}(L)/\kappa$, the fact that this ratio fails to reach a well-established physical limit casts severe doubt on the reliability of the whole reconstruction process based on the effective thermal conductivity. The fact that the effective thermal conductivity approach relies on the assumption of diffusive transport, which, in term, implies late times, was discussed in detail in our previous work [19] in the context of the transient thermal grating experiment. Failure to allow for sufficient time for transport to transition to diffusive, will result in an unreliable measurement and a poor reconstruction.

To illustrate the above point further, we consider the special case of one-dimensional transport ($L \rightarrow \infty$) and define a time- and mode-dependent Knudsen number $\text{Kn}_\omega(t) = \Lambda_\omega/\mathcal{D}(t)$ that characterizes the transport regime inside the silicon. Here, $\mathcal{D}(t)$ is the characteristic heat penetration depth. It is defined as the length inside silicon, measured from the Al-Si interface, where the deviational temperature reaches 1% of the initial

deviational temperature, i.e. $\Delta T(\mathcal{D}(t)) = 0.01$ K. Figure 11a shows the mode dependent Knudsen number defined in this way inside silicon. The simulation is based on MC simulations of BTE using Holland silicon properties, experimental transmissivities, and noise-free relaxation profiles for 5 ns (similar to pump-probe experiment) plotted for the duration $35 \text{ ps} \leq t \leq 5 \text{ ns}$ (the 35 ps is chosen since this is the time that the surface temperature of Al starts to decrease from the initial value of $\Delta T(t = 0) = 1$ K, implying that this is the time that the transport regimes begin to be observed in our measurement). The 21 lines in the figure correspond to 20 selected modes of data (there is a total of 1399 modes in the Holland data) and their average, the latter defined as the sum of the weighted Knudsen numbers of different frequencies (weighted by the density of states). We can see in the figure that for a significant number of modes, even at the end of the observation window (~ 5 ns), the Knudsen number is significantly larger than one, implying that diffusive behavior has yet to set in.

In order to further verify that the saturation in κ_{eff} observed in figure 10b is caused by non-diffusive effects, we performed long-time simulations of the 1D problem described above. In these simulations κ_{eff} was extracted at progressively later times, but always within a sampling window of 5 ns duration ($t_{\text{final}} - t_{\text{initial}} = 5$ ns). Figure 11b shows $\kappa_{\text{eff}}(L = \infty)/\kappa$ versus the end of measurement period, t_{final} , for different measurement times for Holland silicon properties, both experimental and DMM transmissivities, and noise-free relaxation profiles. The leftmost points in the figure correspond to a time window of $t_{\text{final}} = 5$ ns, which is the time window used for the reconstruction data of figure 10b; the consistency between these values and the saturated values in figure 10b suggests that our 1D problem is a good representation of the physics of the 2D problem for the larger values of L .

Figure 11b clearly shows that $\kappa_{\text{eff}}(L = \infty)/\kappa \rightarrow 1$ as t_{final} increases, as expected, since transport inside the silicon becomes more diffusive. The figure also shows that the value of $\kappa_{\text{eff}}(L = \infty)/\kappa = 0.92$ observed for the experimental transmissivities is fortuitously high for that particular observation window and returns to values that are consistent with the DMM model for other observation windows. Although this large discrepancy between the values of $\kappa_{\text{eff}}(L \rightarrow \infty)/\kappa$ for the $t_{\text{final}} = 5$ ns window is somewhat fortuitous, it still serves to highlight the sensitivity of the effective thermal conductivity approach on the observation window, which casts serious doubt on its reliability (measurement of a material property should be independent of the measurement window to be considered reliable).

In summary, lack of diffusive behavior in the 2D-dots setup, as seen in figure 11, causes failure of the effective thermal conductivity approach. In contrast, as shown in sections 4.2 - 4.4, the approach proposed here does not suffer from such limitations.

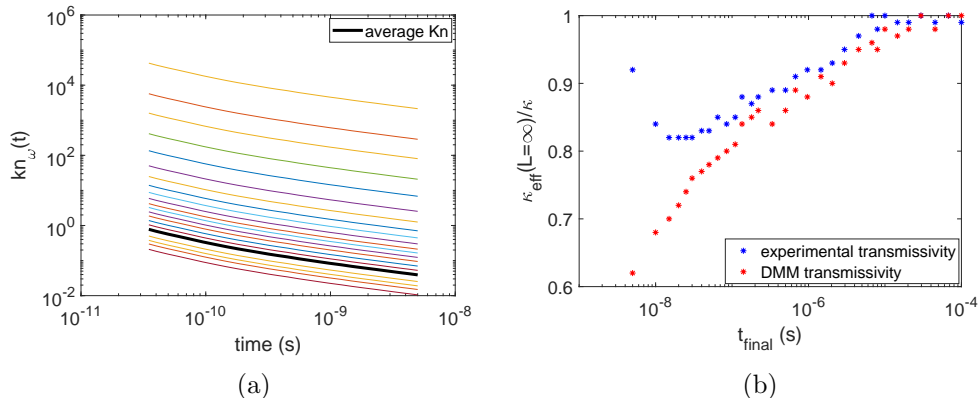


Figure 11: Non-diffusive behavior inside silicon. (a) Mode and time dependent Knudsen number inside silicon for pump-probe measurement time, $0 < t < 5$ ns, based on BTE solution using Holland properties, experimental transmissivities, and noise-free relaxation profiles. (b) Effect of measurement time on transport regime inside silicon for both experimental and DMM transmissivities. The plot shows $\kappa_{\text{eff}}(L = \infty)/\kappa$ for different measurement times. This quantity approaches 1 as the measurement window moves to later times.

5 Summary and outlook

We have proposed and validated an optimization method for reconstructing the relaxation times and free paths from thermal spectroscopy data in the presence of an interface. The reconstruction is achieved by comparing the experimental output with simulations of the BTE, thus avoiding the use of a Fourier assumption or related approximations. The use of MC simulation methods [22–25] to obtain the BTE solutions expands the domain of applicability of the approach, since it does not require the experimental setup to be simple. Our results show that, perhaps surprisingly, the relaxation times can be fully resolved, even if the interface transmissivities are not. This observation is particularly significant for applications where reconstruction of relaxation times is the primary objective, as is the case here, because it implies that various reconstructions previously thought intractable are, in fact, feasible. Although our work has focused on a particular experimental setup, we believe that our conclusions are valid for other experiments in similar transport regimes.

We also note that although for all successful reconstructions shown in this paper the interface conductance (G) was reproduced to a good approximation level, this does not imply that an approximately correct value of G is a sufficient condition for correct reconstruction of relaxation times. In fact, numerical experiments show that simple frequency-independent parametrizations of transmissivities that capture the correct value of G (approximately) but do not reconstruct the relaxation times or predict the thermal behavior correctly are possible. In other words, the “aggregate effect” of the

interface that needs to be captured, extends beyond its (continuum) conductance value. As always, the ultimate gauge of the success (reliability) of the reconstruction is its ability to reproduce the experimental (input) temperature relaxation profiles, measured either via a comparison such as that of figure 8, or via the final value of the objective function.

Complete reconstructions such as the one shown in figure 2 take $O(50)$ hours on a very modest quad core workstation (8 threads on an Intel i7-2600 @ 3.4GHz). In other words, although not cheap, they are certainly feasible, even without powerful computational resources. Owing to the perfect parallel scaling of the kinetic-type MC method [23] used here, wall time can be reduced significantly if multi-CPU parallel computing is utilized. Moreover, the above cost can be significantly reduced by exploiting the robustness of the NM method to noisy inputs, for example, by reducing the number of particles used for the Boltzmann solutions. Although normally the convergence rate of MC simulations is viewed as a poor feature of the method, in this case it can be turned into an advantage by noticing that a reduction of \mathcal{N}_{BTE} by an order of magnitude, resulting in proportionally the same reduction in cost, will only lead to an increase in stochastic error of only $O(3)$ and thus will have only a small effect on the final result accuracy (see figure 2 of [19]). Such, as well as other approaches for reducing the cost of reconstruction will be fully explored in the near future.

The approach proposed here has a number of advantages compared to the effective thermal conductivity (or effective thermal diffusivity) approach. While effective thermal conductivity techniques require the value of the interface thermal conductance as an input to the Fourier heat equation, our algorithm does not make any assumption on that. This not only requires less knowledge of the problem under consideration, it also makes the reconstruction process less susceptible to error. We also recall that, as shown in [19], for an accurate reconstruction of the full spectrum of free paths (and relaxation times) the method proposed here does not require the availability of measurements in all transport regimes, while this is a requirement in the effective-heat-conductivity-based approaches. This requirement is particularly problematic in the 2D-dots experiment where regardless of the value of the chosen length scale L , the regime is never diffusive, as discussed in section 4.5.

Our method was validated using numerical experiments based on the 2D-dots geometry [7] due to its relevance to the current state of the art. In concert with the experimental process, the metal dot height has been assumed constant (100 nm) [29]. However, as discussed in section 4.4, our results suggest that the fixed dot height limits the amount of information that can be extracted for the purpose of reconstructing the interface properties. Preliminary results indicate that more accurate characterization of interface transmissivities is possible if information from (numerical) experiments with variable dot heights is used. In the future, we plan to study the role that different metal film heights play in the reconstruction of interface properties, as well as more generally search for approaches which amplify the sensitivity of reconstruction process to transmissivities, leading to more accurate prediction of the latter.

Acknowledgment

The authors would like to thank G. Chen, V. Chiloyan, S. C. Huberman, Y. M. Marzouk, A. A. Maznev and J.-P. M. Péraud for many useful comments and discussions. This work was supported by the Solid-State Solar-Thermal Energy Conversion Center (S3TEC), an Energy Frontier Research Center funded by the U.S. Department of Energy, Office of Science, Basic Energy Sciences under Award# DE-SC0001299 and DE-FG02-09ER46577. The authors would also like to thank the anonymous referees for numerous suggestions that led to a much improved manuscript.

References

- [1] D. P. SELLAN, J. E. TURNEY, A. J. H. MCGAUGHEY, AND C. H. AMON, *Journal of Applied Physics* 108, 113524 (2010).
- [2] F. YANG AND C. DAMES, *Physical Review B* 91, 165311 (2015).
- [3] K. T. REGNER, A. J. H. MCGAUGHEY, AND J. A. MALEN, *Physical Review B* 90, 064302 (2014).
- [4] A. A. MAZNEV, J. A. JOHNSON, AND K. A. NELSON, *Physical Review B* 84, 195206 (2011).
- [5] A. J. MINNICH, J. A. JOHNSON, A. J. SCHMIDT, K. ESFARJANI, M. S. DRESSELHAUS, K. A. NELSON, AND G. CHEN, *Physical Review Letters* 107, 095901 (2011).
- [6] A. J. MINNICH, *Physical Review Letters* 109, 205901 (2012).
- [7] Y. HU, L. ZENG, A. J. MINNICH, M. S. DRESSELHAUS, AND G. CHEN, *Nature Nanotechnology* 10, 701-706 (2015).
- [8] J.-K. YU, S. MITROVIC, D. THAM, J. VARGHESE, AND J. R. HEATH, *Nature Nanotechnology* 5, 718-721 (2010).
- [9] M. C. WINGERT, Z. C. Y. CHEN, E. DECHAUMPHAI, J. MOON, J.-H. KIM, J. XIANG, AND R. CHEN, *Nano Letters* 11, 5507-5513 (2011).
- [10] E. POP, S. SINHA, AND K. E. GOODSON, *proceedings of the IEEE* 94, 1587-1601 (2006).
- [11] D. G. CAHILL, K. GOODSON, AND A. MAJUMDAR, *Journal of Heat Transfer* 124, 223-241 (2001).
- [12] S.-M. LEE AND D. G. CAHILL, *Journal of Applied Physics* 81, 2590 (1997).

- [13] K. BISWAS, J. HE, I. D. BLUM, C.-I WU, T. P. HOGAN, D. N. SEIDMAN, V. P. DRAVID, AND M. G. KANATZIDIS, *Nature* 489, 414-418 (2012).
- [14] A. I. HOCHBAUM, R. CHEN, R. D. DELGADO, W. LIANG, E. C. GARNETT, M. NAJARIAN, A. MAJUMDAR, AND P. YANG, *Nature* 451, 163-167 (2008).
- [15] A. I. BOUKAI, Y. BUNIMOVICH, J. TAHIR-KHELI, J.-K. YU, W. A. GODDARD III, AND J. R. HEATH, *Nature* 451, 168-171 (2008).
- [16] Z. TIAN, S. LEE, G. CHEN, *Journal of Heat Transfer* 135, 061605 (2013).
- [17] M. ZEBARJADI, K. ESFARJANI, M. S. DRESSELHAUS, Z. F. REN, AND G. CHEN, *Energy and Environmental Science* 5, 5147-5162 (2012).
- [18] D. KRAEMER, B. POUDEL, H.-P. FENG, J. C. CAYLOR, B. YU, X. YAN, Y. MA, X. WANG, D. WANG, A. MUTO, K. MCENANEY, M. CHIESA, Z. REN, AND G. CHEN, *Nature Materials* 10, 532-538 (2011).
- [19] M. FORGHANI, N. G. HADJICONSTANTINOY, AND J.-P. M. PÉRAUD, *Physical Review B* 94, 155439 (2016).
- [20] J. A. ROGERS, Y. YANG, AND K. A. NELSON, *Applied Physics A* 58, 523-534 (1994).
- [21] K. C. COLLINS, A. A. MAZNEV, Z. TIAN, K. ESFARJANI, K. A. NELSON, AND G. CHEN, *Journal of Applied Physics* 114, 104302 (2013).
- [22] J.-P. M. PÉRAUD AND N. G. HADJICONSTANTINOY, *Physical Review B* 84, 205331 (2011).
- [23] J.-P. M. PÉRAUD AND N. G. HADJICONSTANTINOY, *Applied Physics Letters* 101, 153114 (2012).
- [24] J.-P. M. PÉRAUD, C. D. LANDON, AND N. G. HADJICONSTANTINOY, *Annual Review of Heat Transfer* 17, 205-265 (2014).
- [25] J.-P. M. PÉRAUD AND N. G. HADJICONSTANTINOY, *Physical Review B* 91, 235321 (2015).
- [26] D. G. CAHILL, W. K. FORD, K. E. GOODSON, G. D. MAHAN, A. MAJUMDAR, H. J. MARIS, R. MERLIN, AND S. R. PHILLPOT, *Journal of Applied Physics* 93, 793 (2003).
- [27] D. G. CAHILL, P. V. BRAUN, G. CHEN, D. R. CLARKE, S. FAN, K. E. GOODSON, P. KEBLINSKI, W. P. KING, G. D. MAHAN, A. MAJUMDAR, H. J. MARIS, S. R. PHILLPOT, E. POP, AND L. SHI, *Applied Physics Reviews* 1, 011305 (2014).

- [28] M. E. SIEMENS, Q. LI, R. YANG, K. A. NELSON, E. H. ANDERSON, M. M. MURNANE, AND H. C. KAPTEYN, *Nature Materials* 9, 26-30 (2010).
- [29] K. M. HOOGEBOOM-POT, J. N. HERNANDEZ-CHARPAK, X. GU, T. D. FRAZER, E. H. ANDERSON, W. CHAO, R. W. FALCONE, R. YANG, M. M. MURNANE, H. C. KAPTEYN, AND D. NARDI, *Proceedings of the National Academy of Sciences USA* 112, 4846-4851 (2015).
- [30] E. T. SWARTZ AND R. O. POHL, *Reviews of Modern Physics* 61, 605 (1989).
- [31] A. J. MINNICH, G. CHEN, S. MANSOOR, AND B. S. YILBAS, *Physical Review B* 84, 235207 (2011).
- [32] A. J. MINNICH, PhD thesis, Massachusetts Institute of Technology, Cambridge, MA (2011).
- [33] A. S. HENRY AND G. CHEN, *Journal of Computational and Theoretical Nanoscience* 5, 141-152 (2008).
- [34] W. A. LITTLE, *Canadian Journal of Physics* 37, 334-349 (1959).
- [35] C. HUA, X. CHEN, N. K. RAVICHANDRAN, AND A. J. MINNICH, *Physical Review B* 95, 205423 (2017).
- [36] J. A. NELDER AND R. MEAD, *The Computer Journal* 7, 308-313, (1965).
- [37] E. HAZAN, K. Y. LEVY, AND S. SHALEV-SHWARTZ, *Proceedings of the 33rd International Conference on Machine Learning* 48, 1833-1841 (2016).
- [38] K. ESFARJANI, G. CHEN, AND H. T. STOKES, *Physical Review B* 84, 085204 (2011).
- [39] R. STEDMAN AND G. NILSSON, *Physical Review* 145, 492 (1966).
- [40] D. LI AND A. J. H. MCGAUGHEY, *Nanoscale and Microscale Thermophysical Engineering* 19, 166-182 (2015).

Appendix A: Parameters of piece-wise linear model for relaxation times

Relationship (8) is constructed such that the intersections of the piecewise linear segments at ω_j^S , $j = 1, \dots, M - 1$, are smoothed by third-order polynomial functions. Each

smoothing polynomial extends over a frequency range of 2Δ , centered on ω_j^S and denoted by (X_{2j-1}^S, X_{2j}^S) , where

$$\begin{aligned} X_0^S &= \omega_0^S, \\ X_{2j}^S &= \omega_j^S + \Delta, \quad X_{2j-1}^S = \omega_j^S - \Delta, \quad j \in \{1, \dots, M-1\}, \\ X_{2M-1}^S &= \omega_M^S. \end{aligned} \quad (22)$$

In this work, we have used $\Delta = 5 \times 10^{12}$ rad/s. The coefficients a_j^S , b_j^S , c_j^S , and d_j^S are calculated from the following equations

$$\begin{aligned} a_j^S &= -\frac{\log\left(1 - \left(\frac{\Delta}{\omega_j^S}\right)^2\right)}{\left[\log\left(\frac{\omega_j^S + \Delta}{\omega_j^S - \Delta}\right)\right]^3} \left[\frac{\log\left(\frac{\tau_{\omega_{j+1}}^S}{\tau_{\omega_j^S}^S}\right)}{\log\left(\frac{\omega_{j+1}^S}{\omega_j^S}\right)} - \frac{\log\left(\frac{\tau_{\omega_j^S}^S}{\tau_{\omega_{j-1}}^S}\right)}{\log\left(\frac{\omega_j^S}{\omega_{j-1}^S}\right)} \right], \\ b_j^S &= 0.5 \left\{ \frac{1}{\log\left(\frac{\omega_j^S + \Delta}{\omega_j^S - \Delta}\right)} \left[\frac{\log\left(\frac{\tau_{\omega_{j+1}}^S}{\tau_{\omega_j^S}^S}\right)}{\log\left(\frac{\omega_{j+1}^S}{\omega_j^S}\right)} - \frac{\log\left(\frac{\tau_{\omega_j^S}^S}{\tau_{\omega_{j-1}}^S}\right)}{\log\left(\frac{\omega_j^S}{\omega_{j-1}^S}\right)} \right] - 3a_j^S \log\left((\omega_j^S)^2 - \Delta^2\right) \right\}, \\ c_j^S &= \frac{\log\left(\frac{\tau_{\omega_j^S}^S}{\tau_{\omega_{j-1}}^S}\right)}{\log\left(\frac{\omega_j^S}{\omega_{j-1}^S}\right)} - 3a_j^S [\log(\omega_j^S - \Delta)]^2 - 2b_j^S \log(\omega_j^S - \Delta), \\ d_j^S &= \log(\tau_{\omega_{j-1}}^S) - \log(\omega_{j-1}^S) \frac{\log\left(\frac{\tau_{\omega_j^S}^S}{\tau_{\omega_{j-1}}^S}\right)}{\log\left(\frac{\omega_j^S}{\omega_{j-1}^S}\right)} + \\ &\quad 0.5 \frac{[\log(\omega_j^S - \Delta)]^2}{\log\left(\frac{\omega_j^S + \Delta}{\omega_j^S - \Delta}\right)} \left[\frac{\log\left(\frac{\tau_{\omega_{j+1}}^S}{\tau_{\omega_j^S}^S}\right)}{\log\left(\frac{\omega_{j+1}^S}{\omega_j^S}\right)} - \frac{\log\left(\frac{\tau_{\omega_j^S}^S}{\tau_{\omega_{j-1}}^S}\right)}{\log\left(\frac{\omega_j^S}{\omega_{j-1}^S}\right)} \right] - \\ &\quad 0.5a_j^S [\log(\omega_j^S - \Delta)]^2 [3\log(\omega_j^S + \Delta) - \log(\omega_j^S - \Delta)], \end{aligned} \quad (23)$$

where $j \in \{1, \dots, M-1\}$ and $S \in \{LA, TA_1, TA_2\}$.

Appendix B: Parameters of piece-wise linear model for transmissivities

The role of \bar{X}_j^S is similar to X_j^S in equation (22), therefore,

$$\begin{aligned} \bar{X}_0^S &= \bar{\omega}_0^S, \\ \bar{X}_{2j}^S &= \bar{\omega}_j^S + \Delta, \quad \bar{X}_{2j-1}^S = \bar{\omega}_j^S - \Delta, \quad j \in \{1, \dots, \bar{M} - 1\}, \\ \bar{X}_{2\bar{M}-1}^S &= \bar{\omega}_{\bar{M}}^S. \end{aligned} \quad (24)$$

The coefficients \bar{a}_j^S , \bar{b}_j^S , \bar{c}_j^S , and \bar{d}_j^S are calculated from the following equations

$$\begin{aligned} \bar{a}_j^S &= 0, \\ \bar{b}_j^S &= \frac{\frac{T_{12, \bar{\omega}_{j+1}}^S - T_{12, \bar{\omega}_j}^S}{\bar{\omega}_{j+1}^S - \bar{\omega}_j^S} - \frac{T_{12, \bar{\omega}_j}^S - T_{12, \bar{\omega}_{j-1}}^S}{\bar{\omega}_j^S - \bar{\omega}_{j-1}^S}}{4\Delta} - 3\bar{a}_j^S \bar{\omega}_j^S, \\ \bar{c}_j^S &= \frac{T_{12, \bar{\omega}_j}^S - T_{12, \bar{\omega}_{j-1}}^S}{\bar{\omega}_j^S - \bar{\omega}_{j-1}^S} - 3\bar{a}_j^S (\bar{\omega}_j^S - \Delta)^2 - 2\bar{b}_j^S (\bar{\omega}_j^S - \Delta), \\ \bar{d}_j^S &= \frac{T_{12, \bar{\omega}_{j+1}}^S - T_{12, \bar{\omega}_j}^S}{\bar{\omega}_{j+1}^S - \bar{\omega}_j^S} \Delta + T_{12, \bar{\omega}_j}^S - \bar{a}_j^S (\bar{\omega}_j^S + \Delta)^3 - \bar{b}_j^S (\bar{\omega}_j^S + \Delta)^2 - \bar{c}_j^S (\bar{\omega}_j^S + \Delta), \end{aligned} \quad (25)$$

where $j \in \{1, \dots, \bar{M} - 1\}$ and $S \in \{LA, TA_1, TA_2\}$. Note that although the matching conditions between the line segments require a third order polynomial, here, due to the symmetrical choice of Δ , the order of polynomial has reduced to two, $\bar{a}_j^S = 0$.